UC Berkeley

UC Berkeley Previously Published Works

Title

Evolution of Protrusions on Lithium Metal Anodes Stabilized by a Solid Block Copolymer Electrolyte Studied Using Time-Resolved X-ray Tomography

Permalink

https://escholarship.org/uc/item/8bh316g3

Journal

ACS Applied Materials & Interfaces, 13(23)

ISSN

1944-8244

Authors

Veeraraghavan, Vijay D

Frenck, Louise

Maslyn, Jacqueline A

et al.

Publication Date

2021-06-16

DOI

10.1021/acsami.1c04582

Peer reviewed

eScholarship.org Powered by the California Digital Library
University of California

Evolution of Protrusions on Lithium Metal Anodes Stabilized by a Solid Block Copolymer Electrolyte Studied Using Time-Resolved X-ray Tomography

Vijay D. Veeraraghavan,[†] Louise Frenck,[†,‡] Jacqueline A. Maslyn,[†,‡] Whitney S. Loo,[†] Dilworth Y. Parkinson,[§] Nitash P. Balsara[*,†,‡]

[†]Department of Chemical and Biomolecular Engineering, University of California, Berkeley, Berkeley, California 94720, United States

[‡]Materials Sciences Division and [§]Advanced Light Source, Lawrence Berkeley National Laboratory, Berkeley, California 94720, United States

KEYWORDS: Lithium dendrite, electrodeposited lithium morphology, polymer electrolyte, salt concentration, polarization time, lithium metal, rechargeable batteries

ABSTRACT: Growing demand for rechargeable batteries with higher energy densities has motivated research focused on enabling the lithium metal anode. A prominent failure mechanism in such batteries is short circuiting due to the uncontrolled propagation of lithium protrusions that often have a dendritic morphology. In this paper, the electrodeposition of metallic lithium through a rigid polystyrene-*b*-poly(ethylene oxide) (PS-*b*-PEO or SEO) block copolymer electrolyte was studied using hard X-ray microtomography. In this system, the protrusions were approximately ellipsoidal globules: we take advantage of this simple geometry to quantify their growth as a function of polarization time and electrolyte salt concentration. The growth of 47 different globules was tracked with time to obtain average velocities of globule growth into the electrolyte. The globule diameter was a linear function of globule height in the electrolyte with a slope of about 6, *independent* of time and electrolyte salt concentration.

INTRODUCTION

Integrating lithium metal anodes could double the maximum achievable specific capacity of rechargeable batteries and accelerate the transition to renewable energy.[1,2] However, despite considerable effort, the decades-long push to enable lithium metal anodes has yet to produce safe batteries with sufficiently high lifetimes.[3,4] Liquid electrolytes used in conventional rechargeable batteries suffer from low coulombic efficiency and are unstable against lithium metal anodes.[5−7] Also, cell failure in lithium metal batteries often occurs catastrophically, with short circuiting lithium protrusions (commonly called “dendrites”)[8−12] spanning the electrolyte and potentially initiating thermal runaway and cell ignition.[13−16] The uneven plating of lithium metal at the electrode-electrolyte interface during charging allows these protrusions to nucleate and grow.[17−19] Solid electrolytes with sufficient mechanical strength offer an opportunity to suppress this protrusion growth through the electrolyte with improved stability against lithium metal. Monroe and Newman laid the theoretical underpinnings of the mechanical suppression of lithium metal protrusions, predicting that a shear modulus twice that of lithium metal would force planar lithium plating and stop protrusion growth.[20−22] Barai *et al*. contributed to this theory by identifying current density distribution as an additional operation parameter to promote stable lithium deposition.[23,24] However, solid electrolytes that meet all of the design requirements of rechargeable batteries with lithium metal anodes have not yet been developed.

Solid block copolymer electrolytes, comprising covalently bound rigid non-conducting and flexible conducting polymer blocks, offer independent control over mechanical strength and electrochemical performance.[25] One extensively studied system is polystyrene-*block*-poly(ethylene oxide),[18,26−37] also referred to as PS-

b-PEO or SEO. Microphase separation results in the formation of rigid, non-conducting polystyrene-rich (PS) domains and soft poly(ethylene oxide)-rich (PEO) domains. The solvation of lithium bis(trifluoromethanesulfonyl)imide lithium salt (LiTFSI) in the PEO-rich[38] domains enables lithium ion transport,[39–41] while having little to no effect on shear modulus.[42] The purpose of this study was to observe the evolution of lithium protrusion growth in SEO/LiTFSI mixtures.

Lithium protrusions come in a variety of morphologies, depending on the shear modulus of the electrolyte and the applied current density.[23,24,43–45] In liquid electrolytes, lithium protrusions take on complex shapes that are often referred to as mossy or dendritic; quantifying the evolution of such structures under an applied current is necessarily complex. In contrast, protrusions formed in SEO electrolytes are, to a good approximation, ellipsoidal globules. The evolution of these protrusions under an applied current can be quantified by monitoring changes in both the height and the width of the globules. This presents an opportunity for fundamental studies on the nature of nonplanar electrodeposition of lithium.

Direct visualization of lithium metal protrusion growth has been achieved by both microscopy[46–50] and tomography.[51,52] Our study is part of a series wherein hard X-ray microtomography is used to visualize the growth of protrusions on lithium metal anodes in contact with SEO electrolytes.[18,32–36] In this paper, we extended our work to cover a wide range of salt concentrations; the ratio of lithium to ethylene oxide monomers, *r*, varies from 0.04 to 0.18. Lithium-SEO-lithium symmetric cells were polarized unidirectionally and tomograms were obtained at selected time intervals (every 50 h) during polarization. Cells were polarized until they failed due to short circuiting; all cell lifetimes exceeded 200 h. At an applied current density of 0.175 mA cm^{-2}, the mean thickness of the electrodeposited lithium layer on the anode was in the vicinity of 200 μm at cell failure. Our experiments enabled tracking of the growth of 47 different lithium globules. We present the first comprehensive quantification of the size distribution of lithium globules, and how globules of different sizes grow during electrodeposition.

EXPERIMENTAL SECTION

Materials. The polystyrene-*b*-poly(ethylene oxide) (SEO) diblock copolymer used in this study was synthesized via anionic polymerization in accordance with a previous work.[35] The characteristics of the SEO sample used are shown in Table 1.

Table 1. Characteristics of the polymer electrolytes used in this study.

Name	M_{PS} [kg mol^{-1}]	M_{PEO} [kg mol^{-1}]	PDI	$r = ¿¿$
SEO(235-222)	235	222	1.05	0.04
				0.085
				0.12
				0.15
				0.18

The polydispersity index of this polymer was measured in anhydrous *N*-methyl-2-pyrrolidone (NMP; Sigma Aldrich) with respect to a PS standard. We define electrolyte salt concentration *r* as the molar ratio of Li^+ ions to ethylene oxide groups in PEO. Previous studies have confirmed the presence of a lamellar microstructure in SEO electrolytes in the composition range covered in this study.[35,37,40,42,53] Lithium metal foil (99.9% purity; FMC Lithium) and nickel foil were used for the electrode material in constructed lithium-SEO-lithium symmetric cells. To avoid contamination, all electrolyte preparation and lithium cell assembly was carried out inside an argon-filled glovebox with H_2O and O_2 levels less than 1 ppm.

Electrolyte Preparation. SEO samples were dissolved in anhydrous NMP and mixed with LiTFSI in ratios to give electrolyte salt concentrations in accordance with Table 1 (r = 0.04, 0.085, 0.12, 0.15, and 0.18) at 70 °C for 2 hours. To create a 50 μm-thick electrolyte film upon solvent evaporation, the mixture was drop-casted on a nickel foil-covered solvent caster held under vacuum and left to dry at 60 °C for 12 h. The electrolyte membranes were then peeled from the nickel foil and transferred using an argon-filled desiccator to the antechamber of another glovebox, where they were dried further at 90 °C under active vacuum for over 48 h to ensure complete evaporation of the solvent. The dried membranes were then transferred from the antechamber into the glovebox for cell assembly.

Lithium-SEO-Lithium Symmetric Cell Assembly. A 7/16 in. diameter circular punch was used on the dried SEO membranes to create electrolyte disks for lithium-SEO-lithium symmetric cells. Electrode material consisted of five sheets of 150 μm-thick lithium metal foil

stacked on top of a piece of nickel foil and pressed with a pneumatic press at 130 MPa until the lithium metal was shiny. Two 750 µm-thick lithium electrodes per cell were obtained using a 3/8 in. diameter punch from the electrode material. The SEO electrolyte was flanked by an electrode on either side. Then, the lithium-SEO-lithium stack was sandwiched by two 0.25 mm-thick stainless steel shims to keep the cell flat. An aluminum current collector tab was attached to each of the stainless steel shims and the cell was vacuum sealed in polypropylene-lined aluminum pouch material (Showa-Denko). The cell architecture is shown in Figure S1. One lithium-SEO-lithium symmetric cell per salt concentration was constructed.

Conditioning and Polarization. Cells were first annealed for 4 h at 110 °C followed by 12 h at 120 °C. Cell conditioning and galvanostatic polarization was run at 90 °C in an Associated Environmental Systems SD-402 oven with a Maccor Series 4000 Battery Tester. Preconditioning was achieved with 15 galvanostatic cycles of alternating current direction at a current density of i = 0.02 mA cm^{-2} as described by Maslyn *et al.*[35] Following preconditioning, galvanostatic polarization was performed using an applied unidirectional constant current density at i = 0.175 mA cm^{-2}. At this current density, the expected planar deposition rate of lithium was 0.85 µm h^{-1}. Polarization was paused at t = 10, 60, 110, 160, 210, and 260 h for X-ray microtomography imaging. After each time step and before resuming polarization, cells were allowed to equilibrate at 90 °C for 12 h.

X-ray Microtomography. Hard X-ray microtomography experiments were conducted at Beamline 8.3.2 at the Lawrence Berkeley National Laboratory Advanced Light Source. Monochromatic hard X-rays of energy 22 keV directed at the sample generated X-ray shadows which were converted to visible light using a scintillator before magnification with an optical microscope and conversion to a digital image file. A schematic diagram of this experimental setup is shown in Figure S2. 1313 images were captured at even angle spacing over 180° of sample rotation. These images were reconstructed using Xi-cam software[54] and a Python script to reveal the 3D interior of the cell. X-ray microtomography scans before preconditioning (t = 0 h) and 10 h of polarization were magnified with a 2X lens corresponding to a size of 3.25 µm per pixel and field of view of 8.3 mm x 4 mm. All other scans were magnified with a 4X lens corresponding to a size of 1.62 µm per pixel and a field of view of 4.1 mm x 3.5 mm. Cross-sectional slices were stacked and inspected for key features such as globules and impurity particles using ImageJ software. SEO electrolyte thicknesses were measured before polarization at 10 different locations within each cell to confirm consistent 50 µm-thicknesses for all cells.

RESULTS AND DISCUSSION

Figure 1 shows the typical profile of a lithium-SEO-lithium cell potential, Φ, in response to an applied unidirectional constant current density, i, as a function of polarization time, t. The corresponding expected height for planar lithium deposition at this current density according to Faraday's first law of electrolysis, H_{exp}, and the charge density passed, q, are indicated as secondary x-axes. For all the cells, galvanostatic polarization was paused at increasing time steps over the course of the experiment (t = 10, 60, 110, 160, 210, and 260 h) for imaging using hard X-ray microtomography. Imaging at t = 10 h enabled the identification of most globule nucleation sites, and subsequent 50 h time intervals tracked the evolution of globule size and shape, as well as some instances of globules that nucleated during the later stages of electrodeposition. All of the cells approached a steady-state potential during the different 50 h time intervals, up until a short circuit caused cell failure, at which point the potential dropped to zero (see Figure 1). Galvanostatic polarization at current density i = 0.175 mA cm^{-2} was significantly above the current density threshold previously shown to initiate lithium metal protrusion nucleation in a similar SEO electrolyte,[35] $i_{threshold}$ = 0.04 mA cm^{-2}. Current was applied unidirectionally to avoid the formation of multi-globular protrusion structures, which have been shown to grow during cycling (bidirectional current);[32] quantifying the growth of multi-globular structures would require complicated multi-dimensional tracking. We will soon show that even in the case of isolated globules, three different dimensions must be tracked to quantify globule growth.

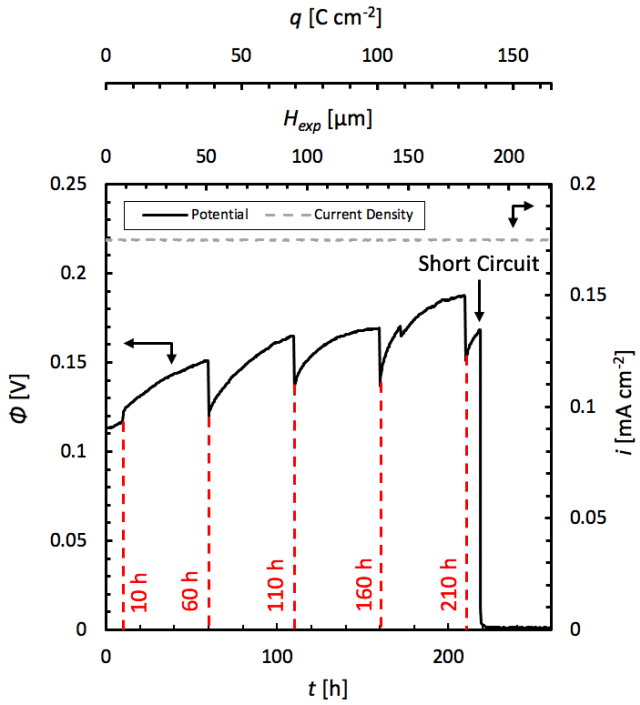

Figure 1. Typical example of unidirectional polarization of a lithium-SEO-lithium symmetric cell (r = 0.12) at a constant current density i = 0.175 mA cm^{-2} and potential response, Φ, as a function of polarization time, t. Secondary y-axes show corresponding expected height for planar lithium deposition, H_{exp}, and charge density passed, q. The cell was imaged after 10 h, subsequent 50 h intervals during which polarization was paused, and cell failure. Failure via short circuit occurred at t = 219 h.

A cross-section of the X-ray tomogram of a preconditioned (t = 0 h) lithium-SEO-lithium symmetric cell is presented in Figure 2. Prior to polarization, the cell was preconditioned using the technique described in the experimental section. Brighter pixels correspond to higher electron density components because they absorb more of the incident X-rays.[32] On the tomograms, thick stacks of darker lithium metal flank either side of the brighter SEO electrolyte. White faceted shapes correspond to impurity particles embedded inside the lithium metal foil. Impurity particles are an intrinsic feature of lithium metal foil with a likely chemical identity of lithium oxide (Li_2O) or lithium hydroxide (LiOH).[32] Previous studies[18,32–35] have shown that most of the lithium protrusions nucleate from impurity particles like the one shown in Figure 2. Importantly, there is no evidence of the nucleation of lithium protrusions after preconditioning and prior to polarization (at t = 0 h) for any of the cells studied.

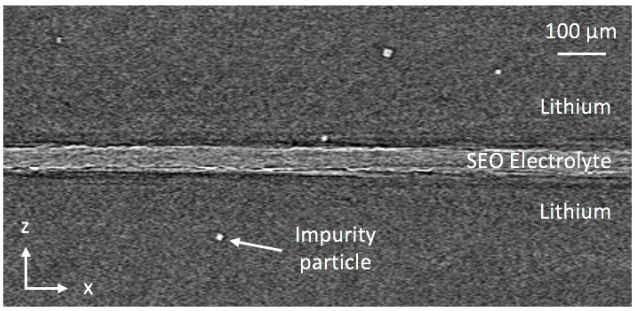

Figure 2. Cross-sectional X-ray microtomography scan in the xz-plane of an unpolarized lithium-SEO-lithium symmetric cell (r = 0.085) after preconditioning (t = 0 h). The cell is composed of an SEO electrolyte (bright middle layer) sandwiched between two stacks of lithium metal (dark stripes). Faceted bright objects correspond to crystalline impurities embedded inside the lithium metal. Images are similar for cells of all salt concentrations.

Figure 3 shows tomograms of a single globular protrusion defect inside one lithium-SEO-lithium symmetric cell (r = 0.085). From nucleation (left) to cell failure (right), Figure 3 illustrates the progression in size and shape of a single short-circuiting globular protrusion over the course of the polarization experiment. Figures 3a to 3f are orthogonal cross-sectional slices of the globule in the xz-plane, and Figures 3g to 3l are slices at the bottom SEO-lithium interface in the xy-plane. Figures of different orientations at the same location and polarization time are organized in vertical columns. For Figures 3a to 3f, the cross-sectional images, lithium metal was plated at the bottom electrode during polarization and this new lithium layer shifted the bottom SEO-lithium interface up. For better visualization, we use the stationary impurity particle at the bottom of the globular protrusion as a reference point and have aligned the tomographic slices accordingly. Figure 3a shows nucleation of the globular protrusion from a face of the impurity particle at t = 10 h, with the majority of globule volume within the SEO electrolyte. Figures 3b to 3f show an increase in globule height, H, the distance from the top face of the impurity particle to the highest point of the globule, over the course of the polarization experiment. The globule is enclosed within a bright structure that we call the “electrolyte sac,” which is composed of the electrolyte’s elements.[32] We observe that most of the globule is growing inside the lithium electrode, i.e., it

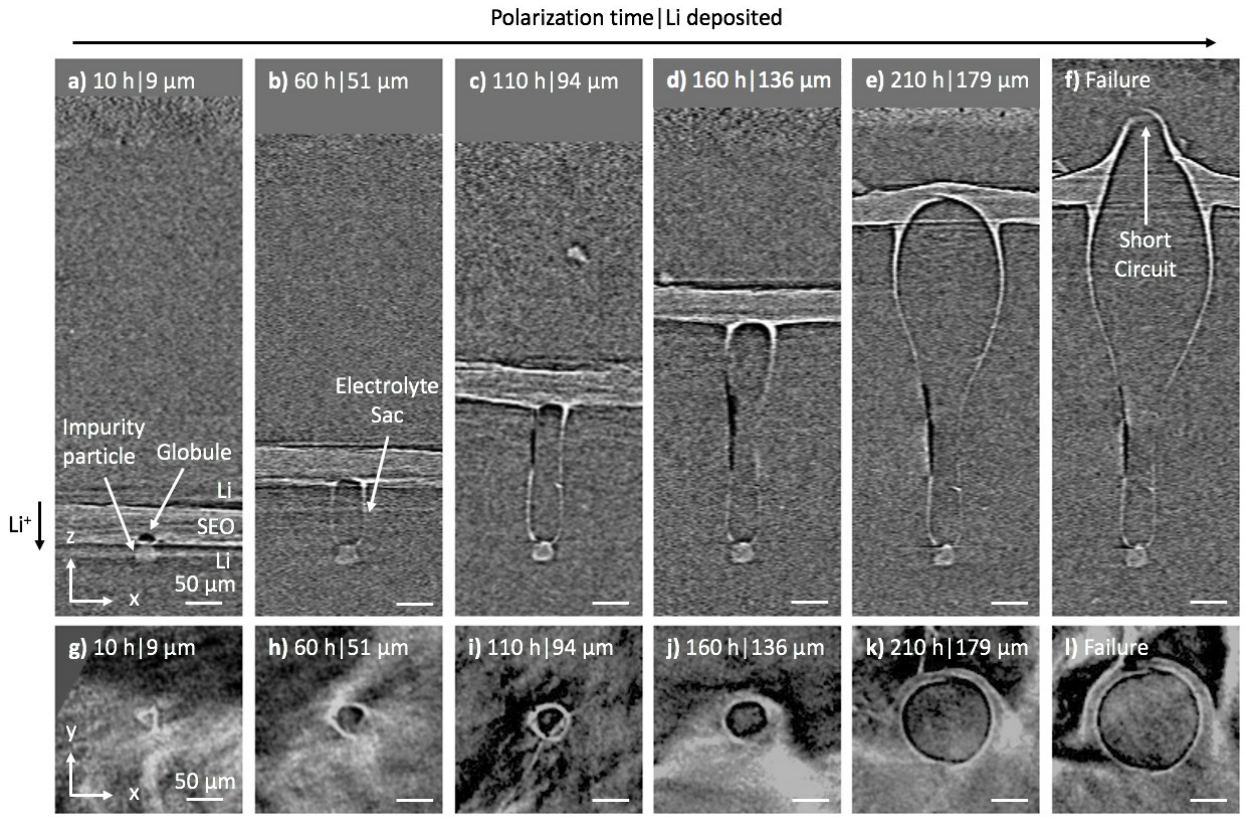

Figure *3*. Time stop imaging of a single lithium protrusion inside a lithium-SEO-lithium symmetric cell (r = 0.085) over the course of a galvanostatic polarization experiment. Left to right tracking of typical dynamics of a single globule as t and q increase. All images are on the same scale. (a-f) Orthogonal cross-sections through the globule in the xz-plane, with lithium plating on the bottom electrode. (a) Globule nucleation from an impurity particle at the SEO-lithium interface. (b-e) Evolution of the globule at increasing polarization time. (f) Full globule penetration of the electrolyte causing failure via short circuit. (g-l) Top view slices in the xy-plane of the bottom SEO-lithium interface at the globule location; columns of images correspond to the same globule at identical t, varying only in orientation.

grows underneath the bottom SEO-lithium interface. However, as the polarization time increases we can clearly see that the globule protrudes into the electrolyte (see Figure 3e). The globule spans the electrolyte in Figure 3f, which causes a short circuit and results in cell failure. It is worth noting that the lithium globule penetrates completely through the electrolyte, from the bottom to the top lithium electrode (same gray value). Figures 3g to 3l exhibit a clear increase in globule interfacial area A as polarization increases. These circular cross-sections of the globule at the electrode-electrolyte interface suggest isotropic growth in the xy-plane. This validates the approximation of globules as ellipsoids, with similar growth from the perspective of both the xz-plane and yz-plane.

We observed the growth of 118 protrusions in cells containing different electrolytes, and tracked 47 in a manner similar to that depicted in Figure 3. All observed lithium protrusion morphologies were globular. Figure 4a shows the areal density of lithium protrusions, P, which was determined by counting the number of globular defects in a cell and normalizing this number by the electrode area as a function of t. The data series represent one cell each at lithium salt concentrations r = 0.04, 0.085, 0.12, 0.15, and 0.18. Error bars of P = 0.2 mm^{-2} were added to each data series, accounting for globules on the edges of a scan which did not appear in subsequent images due to the experimental difficulty in imaging the exact same part of the cell. As in Figure 1, H_{exp} and q, corresponding to a given time, t, are indicated as secondary x-axes. While the majority of globule nucleation seems to occur within the first 60 h for all salt concentrations, it is important to note that nucleation at t > 60 h was observed in all cells. P does not appear to be a systematic function of r. We posit that P is related to the random occurrence of nucleating impurity particles in the electrode located close to the bottom SEO-lithium interface. The largest increase in P between t = 60 h to 210 h occurs for r = 0.15, with P increasing from 0.96 to 1.48 mm^{-2}, or by 54%. During that time, the smallest increase occurs for r = 0.12, with P increasing from 2.07 to 2.29 mm^{-}

^{2}, or 11%. Low salt concentration cells with $r \leq 0.12$ failed at around 200 h; t = 214, 219, and 219 h for r = 0.04, 0.085, and 0.12, respectively. In contrast, high salt concentration cells with $r \geq 0.15$ stayed alive until t = 260 h, the last time step in the experiment. In these cells, a sharp increase in P was observed over a short time between t = 210 and 260 h, from 1.48 to 2.15 mm^{-2} (45%) for r = 0.15 and from 1.55 to 2.29 mm^{-2} (48%) for r = 0.18. Figure 4b normalizes defect density P as a function of t by subtracting the initially measured defect density, P_{60h}. At $t \leq$ 210 h, P-P_{60h} reaches 0.52 mm^{-2}, or a 54% increase in defect density for the r = 0.15 cell. P-P_{60h} for all other salt concentrations increases to 0.22 mm^{-2} over the first 210 h. As in Figure 4a, we witness a sharp increase in the defect density for the $r \geq 0.15$ cells between t = 210 and 260 h. As t increases and lithium is deposited on the bottom electrode, there appears to be no possibility of impurity particles in the bottom electrode near the SEO-lithium interface nucleating globules unless they were previously stuck to the interface. We hypothesize that impurity particles stuck to the SEO-lithium interface can remain

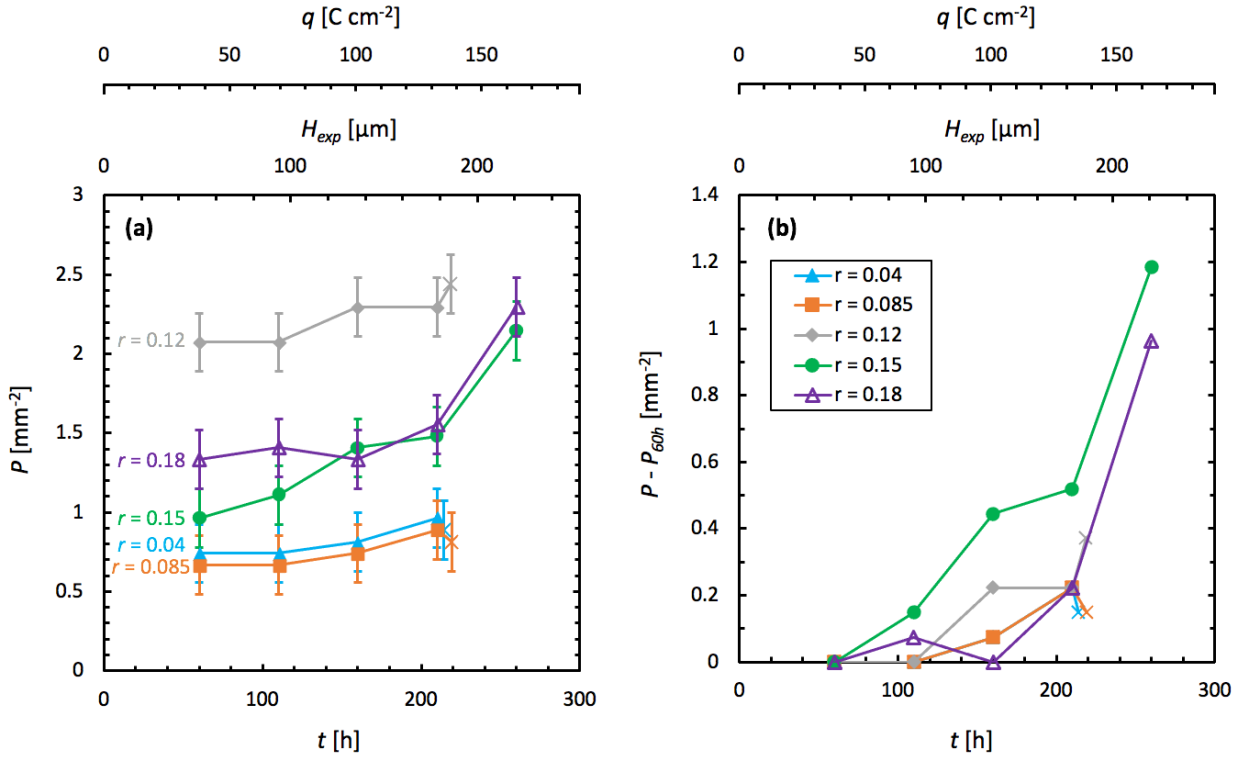

Figure 4. (a) Areal density of lithium protrusions, P, as a function of t, H_e, and q. Data collected from 5 cells at varying lithium salt concentrations, from r = 0.04 to r = 0.18. (b) P – P_{60h}, the areal density of lithium protrusions normalized by subtracting by the initial P value at 60 h, as a function of t, H_e, and q. For all cells, P stays relatively constant with t up to t = 210 h. The cells with a salt concentration of $r \leq 0.12$ fail soon after this time. In contrast, the cells with a salt concentration of $r \geq 0.15$ witness a sharp increase in P with t following t = 210 h and did not fail over the course of the experiment.

dormant until favorable interfacial kinetics allow for nucleation. While most globular defects nucleate from impurity particles at the SEO-lithium interface, Figure 5 presents the evolution in time of a defect formed with no evidence of an impurity particle inside a high salt concentration cell (r = 0.18). The cross-sectional tomograms in the xz-plane shown here are representative of a phenomenon seen only in cells with r = 0.15 and 0.18. We do not see any noticeable features near the bottom SEO-lithium interface at t = 160 h in the region of the cell displayed in Figure 5a. Figure 5b, imaged 50 h later at t = 210 h, emphasizes the growth of a depression in the bottom electrode which is filled by the SEO electrolyte – we refer to this feature as a membrane valley. Following the appearance of this unusual depression, Figure 5c presents the formation of a globule encased within an electrolyte sac 50 h later at t = 260 h. There is clearly a resistance to lithium plating at the membrane valley location. This may be due to salt agglomeration at the SEO-lithium interface or an increase in the interfacial resistance. However, this ionically insulating nature was lost before Figure 5c was acquired. Between t = 210 and 260

h, the valley was filled with a lithium globule that returned the electrolyte thickness to its original value. The rapid increase in P seen between t = 210 and 260 h at high salt concentrations is partly due to the formation of globules within electrolyte valleys.

Figure 6a is a cross-sectional tomogram slice through a globule in the *xz*-plane, and outlines the relevant dimensions associated with quantifying globular morphology. The globule total height, H, is the distance from the top face of the impurity particle to the highest point of the globule, which is normally inside the SEO membrane. H_e is measured from the bottom

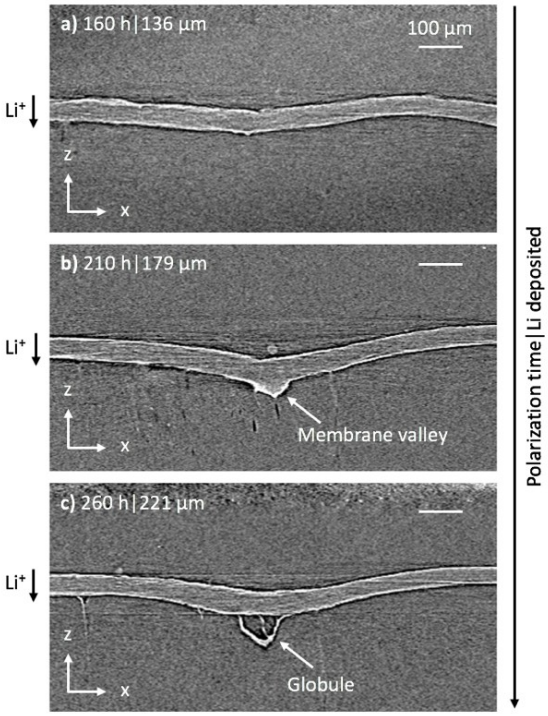

Figure 5. Orthogonal cross-sections in the *xz*-plane of a portion of a high salt concentration cell (r = 0.18) as t increases from (a) to (c). (a) No noticeable membrane features t = 160 h, (b) the same region of interest at t = 210 h with emergence of a membrane valley, and (c) the formation of a globule at t = 260 h. This phenomenon was only observed in cells with $r \geq 0.15$.

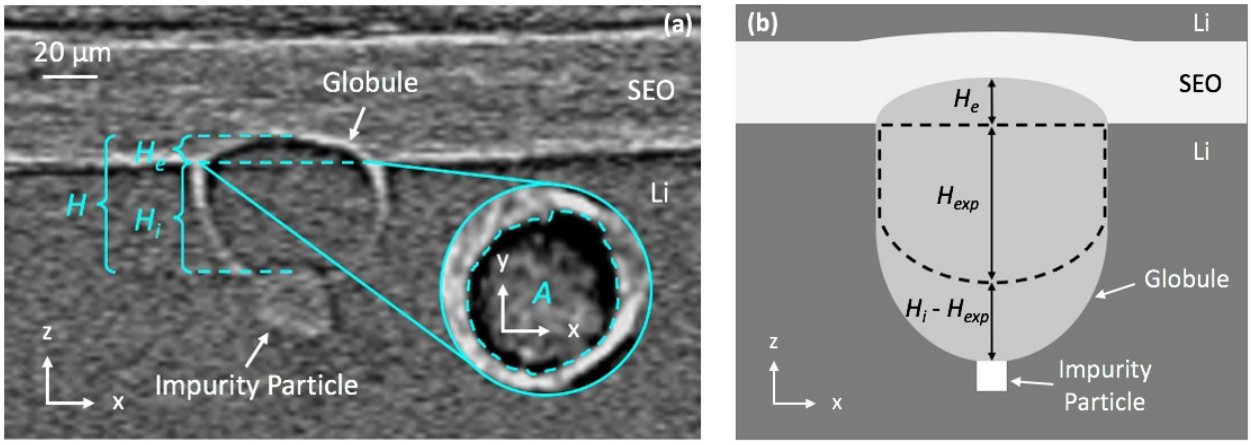

Figure 6. (a) Cross-section in the *xz*-plane through a globule (r = 0.12 cell). Dimensions used to quantify globule total height, H, its components H_e and H_i, and interfacial area, A. H is measured from the top face of the impurity particle to the highest point of the globule, generally within the electrolyte. H_e describes the distance between the bottom SEO-lithium interface and the highest point of the globule. H_i is the distance from the bottom SEO-lithium interface to the lowest point of the globule, or the top face of the impurity particle. The inset shows a top view slice in the *xy*-plane of the bottom SEO-lithium interface at the globule location to show A. (b) Diagram of H_e, expected height from Faraday's law of electrolysis H_{exp}, and $H_i - H_{exp}$ in the *xz*-plane through a typical globule. The diagram depicts reference points for the globule height dimensions: the bottom SEO-lithium interface for H_e, and the expected plating height of lithium within the globule for H_i - H_{exp}.

SEO-lithium interface at the globule location to the highest point of the globule. It is a metric for the globule growth into the electrolyte. H_i is defined as the distance from the bottom SEO-

lithium interface at the globule location to the lowest point of the globule, which is located at the top face of the impurity particle and within the lithium metal electrode. H_i is a metric for globule growth within the electrode. The total height of the globule, H, is calculated by $H = H_i + H_e$. We define A to be the area of the globule measured at the bottom SEO-lithium interface (see Figure 6a inset).

H is related to the lithium deposition rate during polarization. As charge is passed through the cell, lithium metal plates on the bottom electrode and shifts the bottom SEO-lithium interface, along with the highest globule point, upward. Meanwhile, the impurity particle position is fixed within the electrode, and thus H increases with polarization time. It is important to note that impurity particles only serve as nucleation sites for globules, and there is no correlation between impurity particle size and globule growth rate. The time dependence of H_e, which reflects the growth of the globule towards the opposite electrode, is governed by electrolyte deformation, the local salt concentration gradient, and the local electric field. The local interelectrode distance near the tip of the protrusion decreases with increasing H_e and the local current density is expected to grow, affecting not only electrolyte ion migration and the salt concentration gradient across electrodes, but stresses within the electrolyte as well.[36] As the globule grows, it deforms the rigid electrolyte, and the stresses that are generated by this distortion provide resistance to growth. Our observation of increasing H_e indicates that the resistance due to electrolyte deformation is smaller in magnitude than the electrochemical driving forces of increased local current density and salt concentration gradient.

Figure 6b is a schematic of a lithium globule that clarifies the definitions of the parameters depicted in Figure 6a. To understand globule growth within the electrode, it is important to compare H_i to the expected height for planar lithium deposition at this current density, H_{exp}. We therefore also show H_{exp} in Figure 6b. We refer to the difference $H_i - H_{exp}$ as the excess globule growth within the electrode.

Figure 7 tracks globule total height, H, for each individual globule, n, over the course of the experiment (at increasing t), separated by subplots of increasing salt concentration, r. The order of n is unrelated to globule positioning within the cells and is ordered for reasons which will soon be apparent. The different time steps are represented with markers of different colors in Figure 7. The cells with a salt concentration of $r \leq 0.12$ failed shortly after 210 h of polarization, while the cells with a salt concentration of $r \geq 0.15$ stayed alive for the entirety of the experiment, with the final time step at $t = 260$ h. We observe two distinct populations of globules in Figure 7a ($r = 0.04$): the left side of the plot ($n \leq 4$) has a minimum increase in H of -2.1 µm, a maximum increase of 19.5 µm, and an average increase of 3.7 µm over single 50 h time steps; the right side of the plot ($n \geq 5$) has a minimum increase in H of 30.8 µm, a maximum increase of 60.4 µm, and an average increase of 51.3 µm over single 50 h time steps. This distinction is also apparent in Figures 7b to 7e. As a result, slow and fast growing globules are distinguished by slow and fast increases in H over the course of the experiment using orange and green shaded backgrounds, respectively, on each of the plots. Any globule with an increase in H of less than 20 µm over any 50 h time step is designated a slow growing globule, and all other globules are classified as fast growing. Slow growing globules are more prevalent at lower salt concentrations $r = 0.04$ and $r = 0.085$; however, the globules we observed were predominantly fast growing globules. We observe more consistent increases in H with increasing time for fast growing globules; therefore, the rest of the discussion will focus on this population. A comprehensive analysis of both slow and fast growing globules is outside of the scope of this paper.

Figure 8 shows the distribution of excess growth within the electrode, $H_i - H_{exp}$ (Figure 8a), and growth into the electrolyte, H_e (Figure 8b). These distributions were created using R® statistical software and highlight ranges and outliers as well as

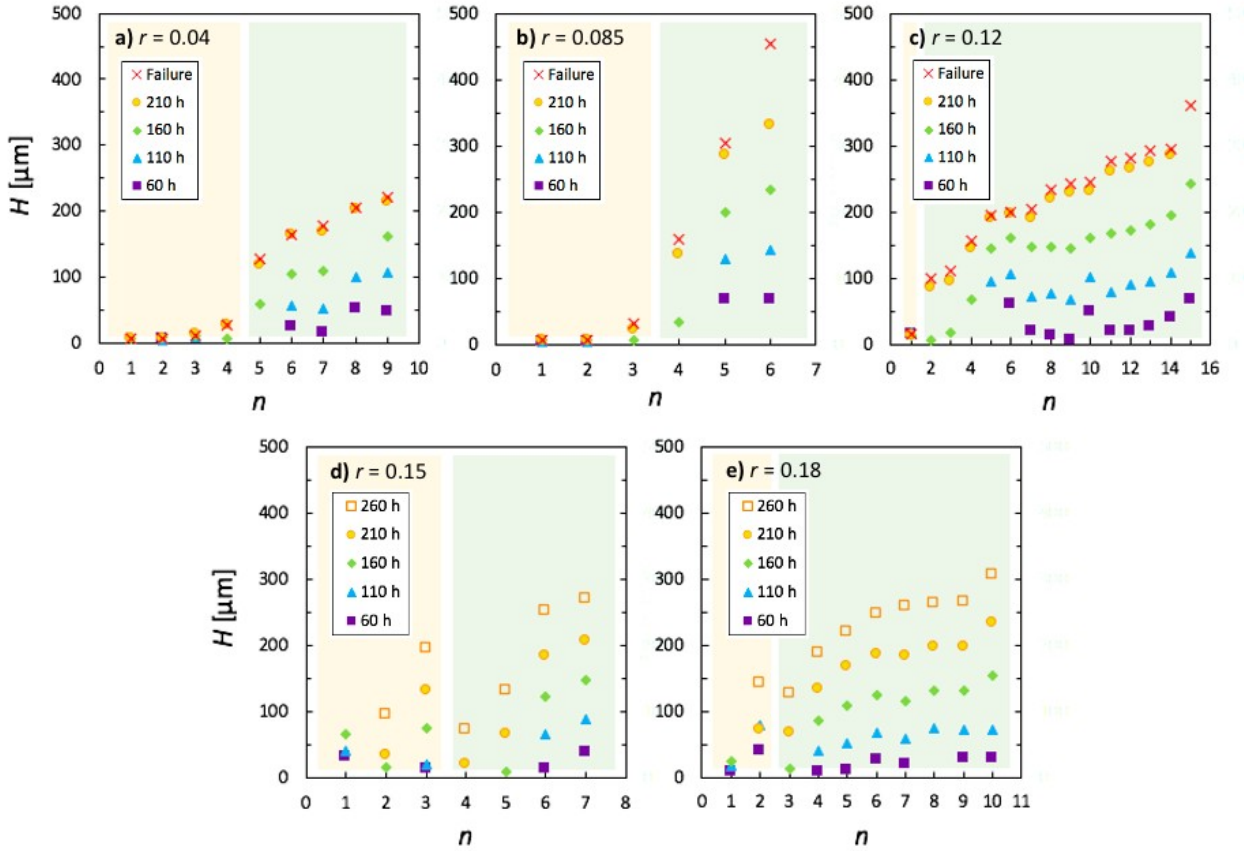

Figure 7. Five subplots (a-e), one at each value of r, track the distribution of H from t = 60 h to cell failure. (a) r = 0.04, (b) r = 0.085, (c) r = 0.12, (d) r = 0.15, (e) and r = 0.18 subplots. There is a clear distinction between slow-growing globules, with little change in H over t, and fast-growing globules which change in H consistently with t. Orange and green backgrounds distinguish slow and fast growing globules, respectively. H increases consistently with t for fast growing globules.

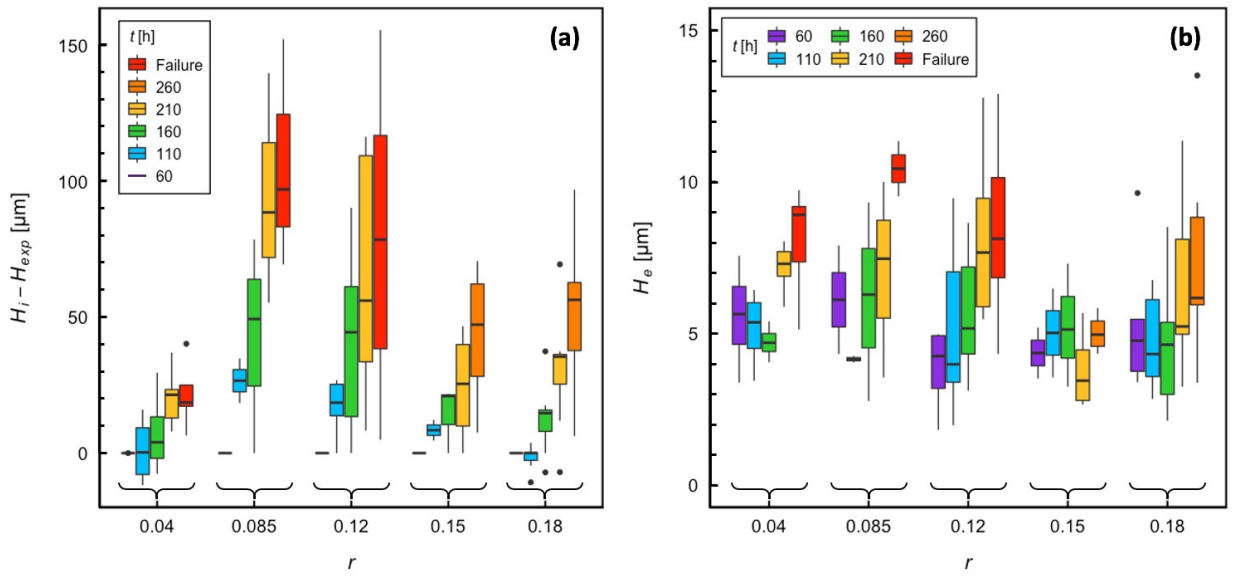

Figure 8. (a) Distribution of excess globule growth within the electrolyte, H_i - H_{exp}, relative to the reference frame of expected height of planar lithium deposition, grouped by r at varying t. (b) Distribution of H_e, the distance from the bottom SEO-lithium interface at the globule location to the highest point of the globule, grouped by r at varying t. Boxplots show the median with a bold line, first and third quartiles with the colored

box bounds, and range with extended lines. Outliers are shown with black dots. Distributions show H_e values that increase with t but have no dependence on r.

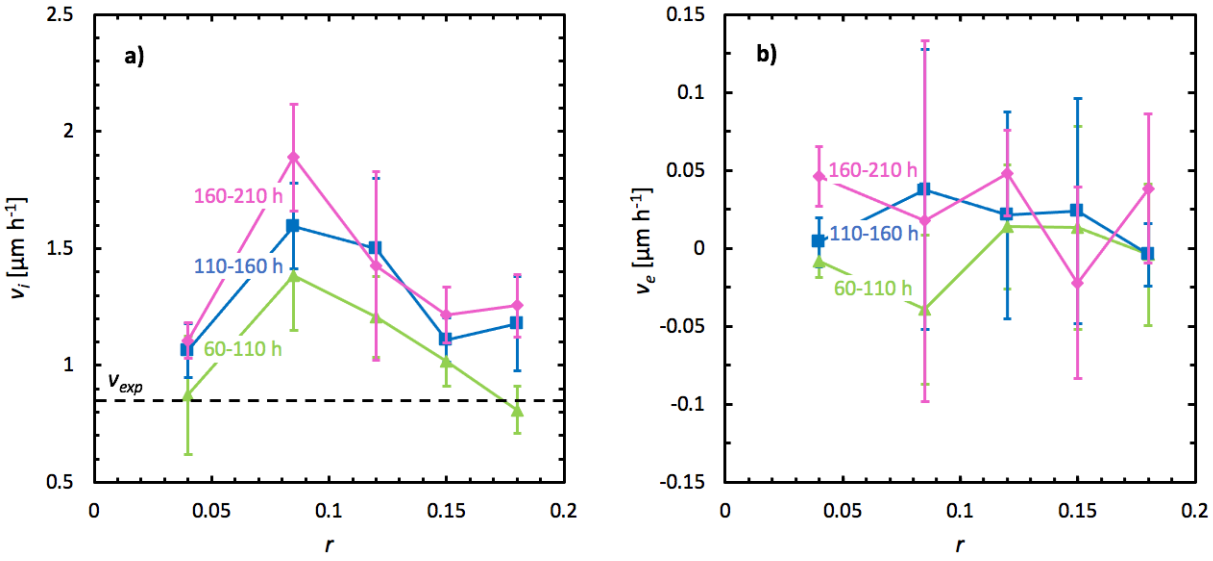

Figure 9. Lithium plating velocities within the electrode and electrolyte, v_i and v_e, respectively, as a function of r, measured over time ranges t_1 to t_2. We define $v_i = [H_i(t_2) - H_i(t_1)]/[t_2 - t_1]$ and $v_e = [H_e(t_2) - H_e(t_1)]/[t_2 - t_1]$. (a) Lithium plating velocity within the electrode, v_i, calculated from H_i, compared to (b) lithium plating velocity into the electrolyte, v_e, calculated from H_e. Values are averages and error bars represent the standard deviation. v_{exp} = 0.85 μm h^{-1} is the expected lithium plating velocity calculated using Faraday's first law of electrolysis and is plotted with a dashed line in (a) for comparison with v_i.

first, second (median), and third quartile values of $H_i - H_{exp}$ and H_e as a function of r for all time steps. The different time steps are represented with identical colors to those in Figure 7. Boxplots show the median with a bold line, first and third quartiles with the colored box bounds, and range with extended black lines. Outliers are shown with black dots and the plots exclude shorting protrusions, which were rarely seen in tomograms and had similar $H_i - H_{exp}$ and much larger H_e values in comparison to typical globules. It is important to note that there are as many as 15 and as few as three data points for a single boxplot. While this may appear limited, we are not aware of any other study where the growth of defects on lithium metal anodes is quantified. Equation 1 describes the excess globule growth relative to the expected plating height of lithium, $H_i - H_{exp}$:

$$H_i - H_{\exp} = H_i - v_{\exp}(t - t_{nuc}), \qquad [1]$$

where v_{exp} = 0.85 μm h^{-1} is the expected lithium plating velocity calculated from Faraday's first law of electrolysis at the applied current density. Our determination of globule geometry is at fixed time points and most of the globules that we have studied nucleated before the t = 60 h scan. We estimate the time at which globules nucleated, t_{nuc}, using Equation 2:

$$t_{nuc} = \frac{v_{\exp} t - H_{i,0}}{v_{\exp}}, \qquad [2]$$

where $H_{i,0}$ is H_i of the first measurable appearance of the globule in X-ray microtomography scans. The first scan at t = 10 h was conducted at a lower magnification of 2X (3.25 μm voxel side length) to identify subregions within the cell that contained globules. Our analysis of globule growth begins with t = 60 h scans where we used a higher magnification of 4X (1.62 μm voxel side length) on the chosen subregions. Equations 1 and 2 enforce the condition that $H_i - H_{exp}$ = 0 μm at t = 60 h; a greater proportion (76%) of the globules nucleated before t = 60 h. $H_i - H_{exp}$ increases with t for all salt concentrations. We observe the greatest $H_i - H_{exp}$ at salt concentration r = 0.085 for all time steps, as it increases from a median of 26.6 μm at t = 110 h to 88.5 μm at t = 210 h. The lowest $H_i - H_{exp}$ occurs at salt concentration r = 0.04 for all time steps, as it increases from a median of 0.3 μm at t = 110 h to 21.4 μm at t = 210 h. Figure 8b plots the distribution of H_e as a function of r at all time steps. At r = 0.04, the median value of H_e increases from 5.6 to 8.9 μm between t = 60 h and failure (t = 214 h). Similar increases are seen at r = 0.085 and r = 0.12. The increase in median H_e with time is within experimental error at r = 0.15. A somewhat slower increase in median H_e is observed from 4.8 to 6.2 μm for r = 0.18 between t = 60 and 260 h, respectively.

Discussions of lithium protrusion growth in the literature mainly focus on growth within the

electrolyte. The difference in scales in Figures 8a and 8b is noteworthy in this context. The growth of protrusions within the electrode is shown on a scale from 0 to 150 μm, while that in the electrolyte is shown on a scale from 0 to 15 μm; most of the protrusion growth takes place within the electrode. Despite the large range in excess plating in the electrode in Figure 8a, the SEO electrolyte appears to possess sufficient mechanical strength to arrest globule growth within the electrolyte at around 10 to 15 μm in all cells in Figure 8b.

We decided to further investigate the phenomenon of consistently increasing $H_i - H_{exp}$ with t shown in Figure 8a. By dividing H into its components H_i and H_e, we were able to look for differences in the deposition rate of lithium metal within the electrode and within the electrolyte, respectively. We refer to these deposition rates as lithium plating velocities and define v_i as the velocity within the electrode and v_e as the velocity within the electrolyte. Equations 3 and 4 explain how these plating velocities were calculated from ΔH_i or ΔH_e and Δt at two adjacent time steps, t_1 and t_2:

$$v_i = \frac{H_i(t_2) - H_i(t_1)}{t_2 - t_1}, \qquad [3]$$

$$v_e = \frac{H_e(t_2) - H_e(t_1)}{t_2 - t_1}. \qquad [4]$$

These plating velocities are plotted in Figure 9 as a function of r at adjacent time steps of increasing polarization time. The values shown are averages and the error bars represent the standard deviation. Figure 9a shows a nonmonotonic dependence of rate v_i on r, with an increase of v_i with r up to a maximum at r = 0.085. This maximum lithium plating velocity increases to 1.38 μm h^{-1} between t = 60 and 110 h, 1.60 μm h^{-1} between t = 110 and 160 h, and 1.89 μm h^{-1} between t = 160 and 210 h. As r increases past 0.085, v_i decreases to a minimum of 0.81 μm h^{-1} between t = 60 and 110 h at r = 0.18. At all salt concentrations, v_i increases with t, with the fastest globule growth within the electrode occurring in the time range 160 to 210 h, the time closest to failure by short circuit. Over the time ranges studied, v_i is greater than the expected planar deposition velocity at this applied current density, v_{exp} = 0.85 μm h^{-1}, which is calculated using Faraday's first law of electrolysis. This is noteworthy because we are elevating the plating velocity within the electrode to a higher-than-expected level at the globule location. This observation and the dependence of v_i on r and t calls for further investigation into the relationship between local current density and the mechanical properties of the electrolyte. Figure 9b shows v_e as a function of r and t. Although these lithium plating velocities changed throughout the course of the experiment, v_e is not discernable within error bars and possesses no apparent r dependence. Importantly, the y-axis scale in Figure 9b is much smaller than that in Figure 9a, indicating much slower growth into the electrolyte than within the electrode. Figure 9 suggests that the electrolyte has the requisite mechanical strength to partially resist globule growth through the electrolyte and limit v_e.[20–22]

The above discussion is focused on tomograms of growing globules. It is, perhaps, important to also examine regions of the lithium electrode away from the globules and beneath the globules for comparison. Figure 10a shows an isolated impurity particle far away from globules at t = 60 h. The same impurity particle at t = 160 and 260 h is shown in Figures 10b and 10c. The top tip of the particle was used as a reference to align the three tomograms. The double sided arrow in Figure 10a at t = 60 h represents the initially measured distance between the bottom SEO-lithium interface and top tip of the impurity particle, $H_{i,60h}$. Additional lithium deposition at t = 160 and 260 h in Figures 10b and 10c, respectively, results in an upwards shift in the bottom SEO-lithium interface. The expected location of the electrode-electrolyte interface based on Faraday's first law of electrolysis is indicated by the double sided arrows labeled $H_{exp} - H_{i,60h}$. The difference between the actual and expected electrode-electrolyte interface location increases with time, as demonstrated by the widening of the gap between the two adjacent dashed lines in Figures 10b and 10c. One may view this difference as a measure of plating uncertainty. This uncertainty is comparable to the curvature introduced in the electrolyte layer due to plating. Figure 10d shows a cross-sectional tomogram of a large, fast growing globule at the latest time step, t = 260 h. An impurity particle circled in red is located 77 μm beneath the globule impurity circled in yellow. This convenient impurity placement provides an opportunity to compare how this distance changes at different values of t. Figure 10e compares the evolution of H_i for the three impurity particles circled in Figures 10a through 10d. All H_i values are with respect to the initially measured distance at t = 60 h, $H_{i,60h}$. At early times ($t \leq$ 110 h), plating above all three impurity particles is similar to the expected increase in electrode-electrolyte interface height based on Faraday's first law of electrolysis, which is denoted by the black dashed line in Figure 10e. As t increases, the discrepancy between actual and expected deposition increases. The yellow and red data series

perfectly overlap in Figure 10d, indicating that the yellow and red impurities remain equidistant throughout the polarization experiment. This implies that there is no yielding of lithium metal beneath this globule. Figure 10 shows that the local rate of lithium deposition varies from the expected value based on Faraday's first law of electrolysis both near and far away from globules. The reason for this variation and the complexities that arise due to it, such as the introduction of curvature at the electrode-electrolyte interface, are outside the scope of the present study.

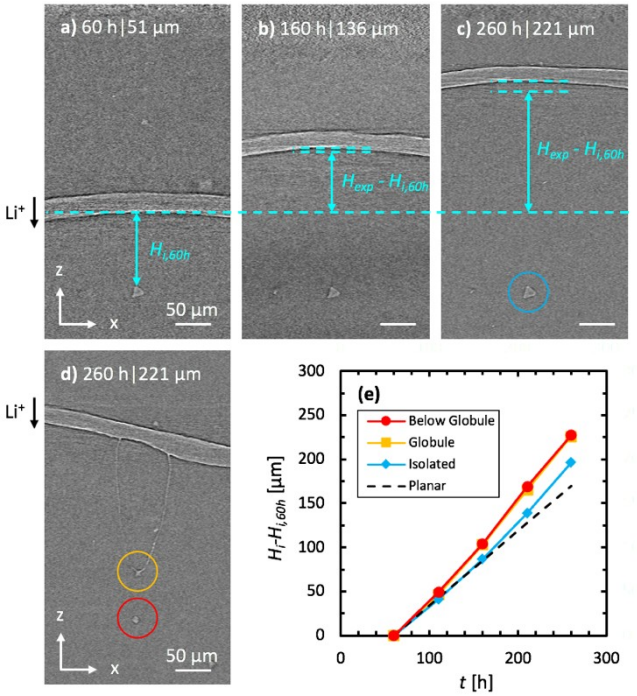

Figure 10. (a-c) Cross-sectional tomograms in the *xz*-plane of the same isolated impurity particle, far from regions of globular growth at t = 60 h, 160 h, and 260 h in the r = 0.18 cell. (a) Initial distance between the bottom SEO-lithium interface and the top face of the isolated impurity particle indicated using $H_{i,60h}$ and the dotted turquoise line across (a), (b), and (c). (b) Expected planar deposition at t = 160 h with respect to the initial location of the impurity particle at t = 60 h using $H_{exp} - H_{i,60h}$. There is a small gap between the actual and expected deposition with respect to this reference indicated with the top two dotted lines. (c) This gap between the actual and expected deposition increases at the latest time step, t = 260 h. (d) Cross-sectional tomogram of a large globule with excess electrode growth with an impurity particle close beneath it. (e) Plot of $H_i - H_{i,60h}$ with t to track lithium deposited for the isolated impurity particle (a-c, blue), globule impurity (d, yellow), and impurity beneath the globule (d, red), taking into account the initial location of the impurity within the electrode at first measurement (60 h). The discrepancy between the actual deposited lithium and expected planar deposition for all impurities is small at early t and is exacerbated as t increases.

We conclude this section by discussing the widening of globules with t. Figure 11 shows a distribution of globule interfacial area, A, on a logarithmic scale as a function of r at increasing t. We observe an exponential increase in A with t for all cells. At low salt concentrations ($r \leq 0.085$), the globule area at early times is larger than that at high salt concentrations ($r \geq 0.12$). However, by the end of the experiment (failure or t = 260 h), we observe similar areas for most of the cells, the exception

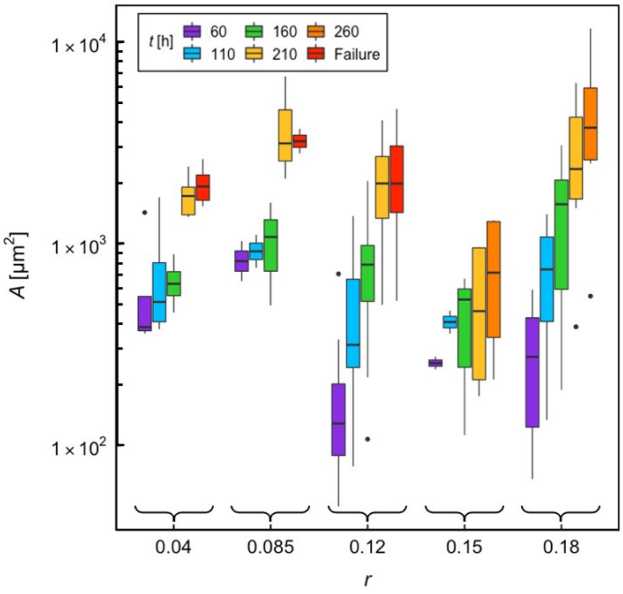

Figure 11. Globule interfacial area, A, distribution plotted on a logarithmic scale and grouped by r at varying t. Boxplots show the median with a bold line, first and third quartiles with the colored box bounds, and range

with extended lines. Outliers are shown with black dots. There is an exponential increase in A with t for all r, with the most pronounced growth at r = 0.18 and least dynamic at r = 0.15.

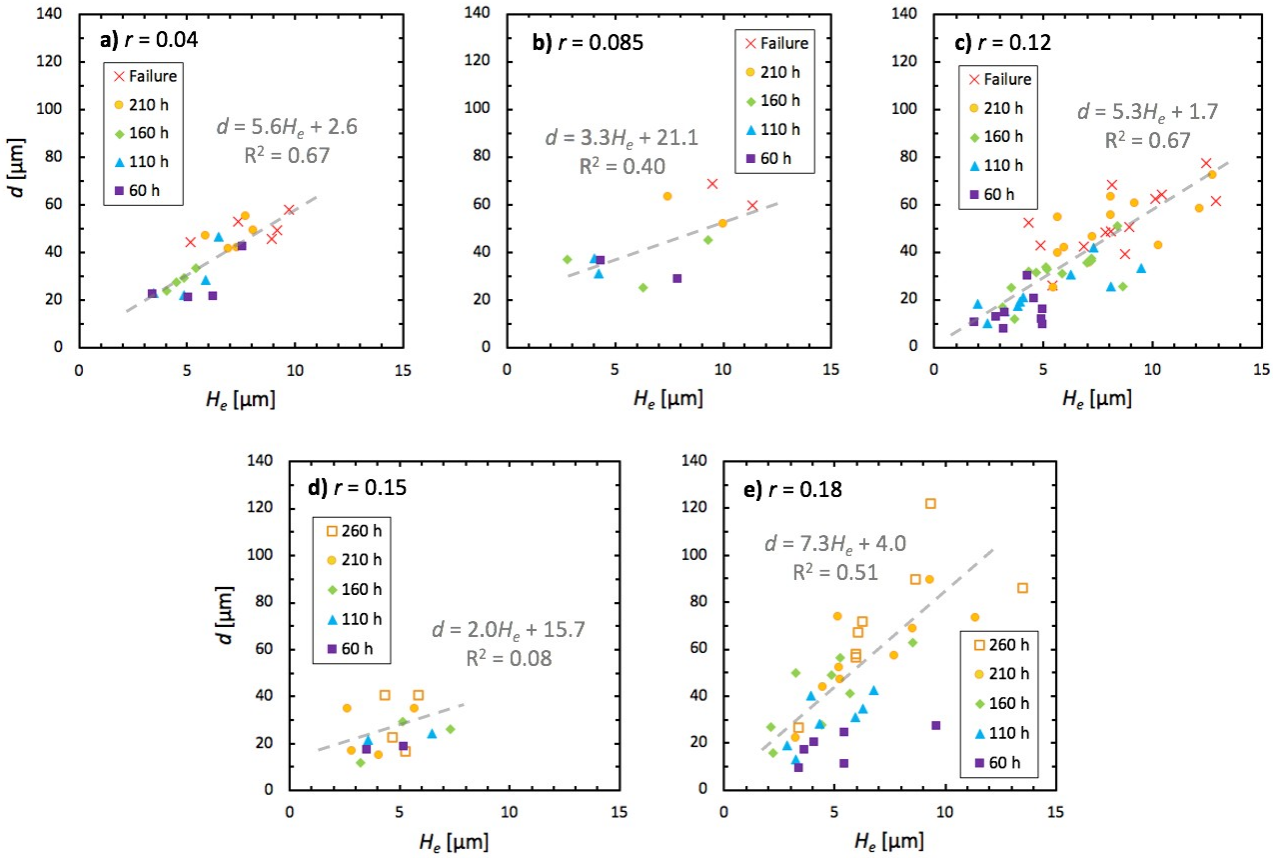

Figure 12. Five subplots, one at each salt concentration, r, to track the correlation between d and H_e from t = 60 h to cell failure for fast growing globules. (a) r = 0.04, (b) r = 0.085, (c) r = 0.12, (d) r = 0.15, (e) and r = 0.18 subplots. A linear regression was performed on all data points across all t for each subplot. d increases linearly with H_e. r = 0.085 and r = 0.15 have the weakest correlation and may be a result of fewer data points. More correlated subplots r = 0.04, 0.085, and 0.18 have similar slopes of 5.6, 5.3, and 7.3, respectively, and indicate little to no dependence of the d to H_e ratio on r or t.

being r = 0.15, which shows a smaller area. Sharp increases in globule area with time are observed at r = 0.12 and 0.18.

Figure 12 displays globule diameter, $d=2\sqrt{A/\pi}$, as a function of globule height within the electrolyte, H_e, for all t and r studied using a subplot for each salt concentration. One linear trendline is fit to each subplot of data. Despite the fact that A (or equivalently d) increases substantially with t in Figure 11, the relationship between d and H_e is presented in Figure 12 without regard to t. For salt concentrations where we were able to track a large number of globules, r = 0.04, 0.12, and 0.18, the slopes of the d versus H_e linear fits are 5.6 ± 0.9, 5.3 ± 0.5, and 7.3 ± 1.2, respectively. These data sets exhibit the strongest correlations with the statistical coefficient of determination, R^2, greater than 0.5. For the salt concentrations where only a few globules were observed, r = 0.085 and 0.15, the slopes of the d versus H_e linear fits are 3.3 ± 1.3, 2.0 ± 1.8, respectively. The intercepts in Figure 12 vary from 1.7 to 21.1 μm. The linearity of d versus H_e for globule growth through an SEO electrolyte was shown by Ho *et al.*,[36] who only examined two failed cells at a fixed salt concentration (r = 0.085). The slope and intercept reported by Ho *et al*. was 2.39 ± 0.12 and 22.4 ± 2.6 μm, respectively. The implication of the data in Figure 12 is that globule growth in block copolymer electrolytes is fundamentally different from dendritic growth in conventional liquid electrolytes. Dendrites are thin, filamentous structures that branch as they grow from the anode towards the cathode. While we are not aware of any systematic attempt to quantify dendrite geometry in detail, there appears to be little change in the diameter of the filaments as dendrites grow. In contrast, globules growing through block copolymer electrolytes flatten substantially as they grow;[34] the average slope of the d versus H_e fits for the three cells with a large number of growing globules is 6.1 ± 1.1. We

attribute this qualitative difference to the fact that the SEO electrolytes exert a stress on the growing protrusions; liquids are incapable of exerting a stress on growing protrusions.

CONCLUSIONS

We prepared lithium-SEO-lithium symmetric cells at varying salt concentrations and imaged them using hard X-ray microtomography at time intervals of 50 h of unidirectional polarization in order to track the evolution of globular defects on the lithium metal electrode. The initial density of globules is independent of salt concentration; variations are a result of the random distribution of impurity particles near the surface of the lithium metal electrodes from which globules nucleate.

We showed the existence of slow and fast growing globules in cells of all salt concentrations. We focused on fast growing globules, as they are more relevant to cell failure. We define three important geometric parameters: the height of the globule in the electrode H_i, the height of the globule in the electrolyte H_e, and the nominal globule diameter, d. All three parameters increase as a function of polarization time, but H_i is about 10 times larger than H_e; most of the globule lies within the electrode. While we find a wide range of globule sizes in each cell, the globule diameter is a linear function of globule height in the electrolyte with a slope of about 6, *independent* of time and electrolyte salt concentration.

The analysis of lithium globule defects formed during polarization presented in this study represents a step toward understanding the factors that impact the lithium metal "dendrite" problem. If we can accurately quantify the dynamics of globule growth and identify the factors that govern it in SEO electrolytes, then we can develop robust models for predicting the nature of electrodeposition on lithium metal anodes. Such models will enable the rational design of polymers and even other condensed phase materials for rechargeable lithium metal batteries.

ASSOCIATED CONTENT

Supporting Information

The Supporting Information is available free of charge on the ACS Publications website.

Schematic diagrams of the cell architecture and X-ray microtomography experimental setup (PDF)

AUTHOR INFORMATION

Corresponding Author

*E-mail: nbalsara@berkeley.edu. Phone: 1-510-642-8973.

ORCID

Vijay D. Veeraraghavan: 0000-0001-7327-7316
Louise Frenck: 0000-0001-7116-2144
Jacqueline A. Maslyn: 0000-0002-6481-2070
Whitney S. Loo: 0000-0002-9773-3571
Dilworth Y. Parkinson: 0000-0002-1817-0716
Nitash P. Balsara: 0000-0002-0106-5565

Author Contributions

J.A.M. and W.S.L. synthesized the SEO block copolymer. V.D.V. and L.F. fabricated the samples and performed the experiments. L.F. performed the microtomography imaging. D.Y.P. and V.D.V. aided in the synchrotron experimental setup. V.D.V. analyzed the data and prepared the figures. V.D.V. and N.P.B. composed the manuscript. N.P.B. directed the work.

Notes

The authors declare no competing financial interest.

ACKNOWLEDGEMENTS

This work was supported by the Assistant Secretary for Energy Efficiency and Renewable Energy, Office of Vehicle Technologies of the U.S. Department of Energy under Contract DE-AC02-05CH11231 under the Advanced Battery Materials Research Program (BMR). L.F. acknowledges funding from the Energy & Biosciences Institute through the EBI-Shell program. Hard X-ray microtomography experiments were performed at the Advanced Light Source, which is supported by the Director, Office of Science, Office of Basic Energy Sciences of the U.S. Department of Energy under contract no. DE-AC02-05CH11231.

ABBREVIATIONS

Φ, potential (V)
A, globule area at the electrode-electrolyte interface (μm^2)
d, globule diameter (μm)
i, applied current density (mA cm^{-2})
H, globule total height (μm)
H_e, globule height into the electrolyte (μm)
H_{exp}, expected planar lithium deposition using Faraday's first law of electrolysis (μm)
H_i, globule height into the electrode (μm)
$H_{i,60h}$, globule height into the electrode after 60 h of polarization time (μm)
Li, lithium
Li_2O, lithium oxide
LiOH, lithium hydroxide
LiTFSI, lithium bis(trifluoromethanesulfonyl) imide
n, tracked globule number
NMP, *N*-methylpyrrolidone
P, areal density of defects (mm^{-2})
P_{60h}, areal density of defects after 60 h of polarization time (mm^{-2})
PEO, poly(ethylene oxide)
PS, polystyrene
q, charge density passed (C cm^{-2})
r, salt concentration
R^2, statistical coefficient of determination
SEO, polystyrene-*b*-poly(ethylene oxide)
t, polarization time (h)
t_{nuc}, estimated time of globule nucleation (h)
v_e, lithium plating velocity into the electrolyte (μm h^{-1})
v_{exp}, expected lithium plating velocity using Faraday's first law of electrolysis (μm h^{-1})
v_i, lithium plating velocity into the electrode (μm h^{-1})

REFERENCES

(1) Chen, S.; Dai, F.; Cai, M. Opportunities and Challenges of High-Energy Lithium Metal Batteries for Electric Vehicle Applications. *ACS Energy Lett.* **2020**, *5* (10), 3140–3151. https://doi.org/10.1021/acsenergylett.0c01545.

(2) Balsara, N. P.; Newman, J. Comparing the Energy Content of Batteries, Fuels, and Materials. *J. Chem. Educ.* **2013**, *90* (4), 446–452. https://doi.org/10.1021/ed3004066.

(3) Yuan, H.; Nai, J.; Tian, H.; Ju, Z.; Zhang, W.; Liu, Y.; Tao, X.; Lou, X. W. (David). An Ultrastable Lithium Metal Anode Enabled by Designed Metal Fluoride Spansules. *Sci. Adv.* **2020**, *6* (10), eaaz3112. https://doi.org/10.1126/sciadv.aaz3112.

(4) Schaefer, J. L.; Lu, Y.; Moganty, S. S.; Agarwal, P.; Jayaprakash, N.; Archer, L. A. Electrolytes for High-Energy Lithium Batteries. *Appl. Nanosci.* **2012**, *2* (2), 91–109. https://doi.org/10.1007/s13204-011-0044-x.

(5) Aurbach, D.; Zinigrad, E.; Cohen, Y.; Teller, H. A Short Review of Failure Mechanisms of Lithium Metal and Lithiated Graphite Anodes in Liquid Electrolyte Solutions. *Solid State Ion.* **2002**, *148*, 405–416.

(6) Xu, W.; Wang, J.; Ding, F.; Chen, X.; Nasybulin, E.; Zhang, Y.; Zhang, J.-G. Lithium Metal Anodes for Rechargeable Batteries. *Energy Env. Sci* **2014**, *7* (2), 513–537. https://doi.org/10.1039/C3EE40795K.

(7) Girard, G. M. A.; Hilder, M.; Dupre, N.; Guyomard, D.; Nucciarone, D.; Whitbread, K.; Zavorine, S.; Moser, M.; Forsyth, M.; MacFarlane, D. R.; Howlett, P. C. Spectroscopic Characterization of the SEI Layer Formed on Lithium Metal Electrodes in Phosphonium Bis(Fluorosulfonyl)Imide Ionic Liquid Electrolytes. *ACS Appl. Mater. Interfaces* **2018**, *10* (7), 6719–6729. https://doi.org/10.1021/acsami.7b18183.

(8) Brissot, C.; Rosso, M.; Chazalviel, J.-N.; Baudry, P.; Lascaud, S. In Situ Study of Dendritic Growth Inlithium/PEO-Salt/Lithium Cells. *Electrochimica Acta* **1998**, *43* (10–11), 1569–1574. https://doi.org/10.1016/S0013-4686(97)10055-X.

(9) Brissot, C.; Rosso, M.; Chazalviel, J. -N.; Lascaud, S. In Situ Concentration Cartography in the Neighborhood of Dendrites Growing in Lithium/Polymer-Electrolyte/Lithium Cells. *J. Electrochem. Soc.* **1999**, *146* (12), 4393–4400. https://doi.org/10.1149/1.1392649.

(10) Brissot, C.; Rosso, M.; Chazalviel, J.-N.; Lascaud, S. Concentration Measurements in Lithium/Polymer–Electrolyte/Lithium Cells during Cycling. *J. Power Sources* **2001**, *94* (2), 212–218. https://doi.org/10.1016/S0378-7753(00)00589-9.

(11) Dollé, M.; Sannier, L.; Beaudoin, B.; Trentin, M.; Tarascon, J.-M. Live Scanning Electron Microscope Observations of Dendritic Growth in Lithium/Polymer Cells. *Electrochem. Solid-State Lett.* **2002**, *5* (12), A286. https://doi.org/10.1149/1.1519970.

(12) Takeda, Y.; Yamamoto, O.; Imanishi, N. Lithium Dendrite Formation on a Lithium Metal Anode from Liquid, Polymer and Solid Electrolytes. *Electrochemistry* **2016**, *84* (4), 210–218. https://doi.org/10.5796/electrochemistry.84.210.

(13) Hou, J.; Lu, L.; Wang, L.; Ohma, A.; Ren, D.; Feng, X.; Li, Y.; Li, Y.; Ootani, I.; Han, X.; Ren, W.; He, X.; Nitta, Y.; Ouyang, M. Thermal Runaway of Lithium-Ion Batteries Employing LiN(SO2F)2-Based Concentrated Electrolytes. *Nat. Commun.* **2020**, *11* (1), 5100. https://doi.org/10.1038/s41467-020-18868-w.

(14) Zhu, Y.; Xie, J.; Pei, A.; Liu, B.; Wu, Y.; Lin, D.; Li, J.; Wang, H.; Chen, H.; Xu, J.; Yang, A.; Wu, C.-L.; Wang, H.; Chen, W.; Cui, Y. Fast Lithium Growth and Short Circuit Induced by Localized-Temperature Hotspots in Lithium Batteries. *Nat. Commun.* **2019**, *10* (1), 2067. https://doi.org/10.1038/s41467-019-09924-1.

(15) Huang, S.; Du, X.; Richter, M.; Ford, J.; Cavalheiro, G. M.; Du, Z.; White, R. T.; Zhang, G. Understanding Li-Ion Cell Internal Short Circuit and Thermal Runaway through Small, Slow and In Situ Sensing Nail Penetration. *J. Electrochem. Soc.* **2020**, *167* (9), 090526. https://doi.org/10.1149/1945-7111/ab8878.

(16) Shin, W.-K.; Kannan, A. G.; Kim, D.-W. Effective Suppression of Dendritic Lithium Growth Using an Ultrathin Coating of Nitrogen and Sulfur Codoped Graphene Nanosheets on Polymer Separator for Lithium Metal Batteries. *ACS Appl. Mater. Interfaces* **2015**, *7* (42), 23700–23707. https://doi.org/10.1021/acsami.5b07730.

(17) Zheng, J.; Kim, M. S.; Tu, Z.; Choudhury, S.; Tang, T.; Archer, L. A. Regulating Electrodeposition Morphology of Lithium: Towards Commercially Relevant Secondary Li Metal Batteries. *Chem. Soc. Rev.* **2020**, *49* (9), 2701–2750. https://doi.org/10.1039/C9CS00883G.

(18) Frenck, L.; Maslyn, J. A.; Loo, W. S.; Parkinson, D. Y.; Balsara, N. P. Impact of Salt Concentration on Nonuniform Lithium Electrodeposition through Rigid Block Copolymer Electrolytes. *ACS Appl. Mater. Interfaces* **2019**, *11* (51), 47878–47885. https://doi.org/10.1021/acsami.9b15606.

(19) Herbert, E. G.; Dudney, N. J.; Rochow, M.; Thole, V.; Hackney, S. A. On the Mechanisms of Stress Relaxation and Intensification at the Lithium/Solid-State Electrolyte Interface. *J. Mater. Res.* **2019**, *34* (21), 3593–3616. https://doi.org/10.1557/jmr.2019.313.

(20) Monroe, C.; Newman, J. Dendrite Growth in Lithium/Polymer Systems. *J. Electrochem. Soc.* **2003**, *150* (10), A1377. https://doi.org/10.1149/1.1606686.

(21) Monroe, C.; Newman, J. The Effect of Interfacial Deformation on Electrodeposition Kinetics. *J. Electrochem. Soc.* **2004**, *151* (6), A880. https://doi.org/10.1149/1.1710893.

(22) Monroe, C.; Newman, J. The Impact of Elastic Deformation on Deposition Kinetics at Lithium/Polymer Interfaces. *J. Electrochem. Soc.* **2005**, *152* (2), A396. https://doi.org/10.1149/1.1850854.

(23) Barai, P.; Higa, K.; Srinivasan, V. Lithium Dendrite Growth Mechanisms in Polymer Electrolytes and Prevention Strategies. *Phys. Chem. Chem. Phys.* **2017**, *19* (31), 20493–20505. https://doi.org/10.1039/C7CP03304D.

(24) Barai, P.; Higa, K.; Srinivasan, V. Effect of Initial State of Lithium on the Propensity for Dendrite Formation: A Theoretical Study. *J. Electrochem. Soc.* **2017**, *164* (2), A180–A189. https://doi.org/10.1149/2.0661702jes.

(25) Bouchet, R.; Maria, S.; Meziane, R.; Aboulaich, A.; Lienafa, L.; Bonnet, J.-P.; Phan, T. N. T.; Bertin, D.; Gigmes, D.; Devaux, D.; Denoyel, R.; Armand, M. Single-Ion BAB Triblock Copolymers as Highly Efficient Electrolytes for Lithium-Metal Batteries. *Nat. Mater.* **2013**, *12* (5), 452–457. https://doi.org/10.1038/nmat3602.

(26) Stone, G. M.; Mullin, S. A.; Teran, A. A.; Hallinan, D. T.; Minor, A. M.; Hexemer, A.; Balsara, N. P. Resolution of the Modulus versus Adhesion Dilemma in Solid Polymer Electrolytes for Rechargeable Lithium Metal Batteries. *J. Electrochem. Soc.* **2012**, *159* (3), A222–A227. https://doi.org/10.1149/2.030203jes.

(27) Panday, A.; Mullin, S.; Gomez, E. D.; Wanakule, N.; Chen, V. L.; Hexemer, A.; Pople, J.; Balsara, N. P. Effect of Molecular Weight and Salt Concentration on Conductivity of Block Copolymer Electrolytes. *Macromolecules* **2009**, *42* (13), 4632–4637. https://doi.org/10.1021/ma900451e.

(28) Hallinan, D. T.; Mullin, S. A.; Stone, G. M.; Balsara, N. P. Lithium Metal Stability in Batteries with Block Copolymer Electrolytes. *J. Electrochem. Soc.* **2013**, *160* (3), A464–A470. https://doi.org/10.1149/2.030303jes.

(29) Metwalli, E.; Rasool, M.; Brunner, S.; Müller-Buschbaum, P. Lithium-Salt-Containing High-Molecular-Weight Polystyrene- *Block* -Polyethylene Oxide Block Copolymer Films. *ChemPhysChem* **2015**, *16* (13), 2882–2889. https://doi.org/10.1002/cphc.201500358.

(30) Niitani, T.; Shimada, M.; Kawamura, K.; Dokko, K.; Rho, Y.-H.; Kanamura, K. Synthesis of Li[Sup +] Ion Conductive PEO-PSt Block Copolymer Electrolyte with Microphase Separation Structure. *Electrochem. Solid-State Lett.* **2005**, *8* (8), A385. https://doi.org/10.1149/1.1940491.

(31) Wang, C.; Sakai, T.; Watanabe, O.; Hirahara, K.; Nakanishi, T. All Solid-State Lithium-Polymer Battery Using a Self-Cross-Linking Polymer Electrolyte. *J. Electrochem. Soc.* **2003**, *150* (9), A1166. https://doi.org/10.1149/1.1593652.

(32) Harry, K. J.; Liao, X.; Parkinson, D. Y.; Minor, A. M.; Balsara, N. P. Electrochemical Deposition and Stripping Behavior of Lithium Metal across a Rigid Block Copolymer Electrolyte Membrane. *J. Electrochem. Soc.* **2015**, *162* (14), A2699–A2706. https://doi.org/10.1149/2.0321514jes.

(33) Harry, K. J.; Hallinan, D. T.; Parkinson, D. Y.; MacDowell, A. A.; Balsara, N. P. Detection of Subsurface Structures underneath Dendrites Formed on Cycled Lithium Metal Electrodes. *Nat. Mater.* **2014**, *13* (1), 69–73. https://doi.org/10.1038/nmat3793.

(34) Harry, K. J.; Higa, K.; Srinivasan, V.; Balsara, N. P. Influence of Electrolyte Modulus on the Local Current Density at a Dendrite Tip on a Lithium Metal Electrode. *J. Electrochem. Soc.* **2016**, *163* (10), A2216–A2224. https://doi.org/10.1149/2.0191610jes.

(35) Maslyn, J. A.; Loo, W. S.; McEntush, K. D.; Oh, H. J.; Harry, K. J.; Parkinson, D. Y.; Balsara, N. P. Growth of Lithium Dendrites and Globules through a Solid Block Copolymer Electrolyte as a Function of Current Density. *J. Phys. Chem. C* **2018**, *122* (47), 26797–26804. https://doi.org/10.1021/acs.jpcc.8b06355.

(36) Ho, A. S.; Barai, P.; Maslyn, J. A.; Frenck, L.; Loo, W. S.; Parkinson, D. Y.; Srinivasan, V.; Balsara, N. P. Uncovering the Relationship between Diameter and Height of Electrodeposited Lithium Protrusions in a Rigid Electrolyte. *ACS Appl. Energy Mater.* **2020**, acsaem.0c01175. https://doi.org/10.1021/acsaem.0c01175.

(37) Schauser, N. S.; Harry, K. J.; Parkinson, D. Y.; Watanabe, H.; Balsara, N. P. Lithium Dendrite Growth in Glassy and Rubbery Nanostructured Block Copolymer Electrolytes. *J. Electrochem. Soc.* **2015**, *162* (3), A398–A405. https://doi.org/10.1149/2.0511503jes.

(38) Fenton, D. E.; Parker, J. M.; Wright, P. V. Complexes of Alkali Metal Ions with Poly(Ethylene Oxide). *Polymer* **1973**, *14* (11), 589. https://doi.org/10.1016/0032-3861(73)90146-8.

(39) Pesko, D. M.; Timachova, K.; Bhattacharya, R.; Smith, M. C.; Villaluenga, I.; Newman, J.; Balsara, N. P. Negative Transference Numbers in Poly(Ethylene Oxide)-Based Electrolytes. *J. Electrochem. Soc.* **2017**, *164* (11), E3569–E3575. https://doi.org/10.1149/2.0581711jes.

(40) Villaluenga, I.; Pesko, D. M.; Timachova, K.; Feng, Z.; Newman, J.; Srinivasan, V.; Balsara, N. P. Negative Stefan-Maxwell Diffusion Coefficients and Complete Electrochemical Transport Characterization of Homopolymer and Block Copolymer Electrolytes. *J. Electrochem. Soc.* **2018**, *165* (11), A2766–A2773. https://doi.org/10.1149/2.0641811jes.

(41) Pożyczka, K.; Marzantowicz, M.; Dygas, J. R.; Krok, F. IONIC CONDUCTIVITY AND LITHIUM TRANSFERENCE NUMBER OF POLY(ETHYLENE OXIDE):LiTFSI SYSTEM. *Electrochimica Acta* **2017**, *227*, 127–135. https://doi.org/10.1016/j.electacta.2016.12.172.

(42) Frenck, L.; Veeraraghavan, V. D.; Maslyn, J. A.; Müller, A.; Ho, A. S.; Loo, W. S.; Minor, A. M.; Balsara, N. P. Effect of Salt Concentration Profiles on Protrusion Growth in Lithium-Polymer-lithium Cells. *Solid State Ion.* **2020**, *358*, 115517. https://doi.org/10.1016/j.ssi.2020.115517.

(43) Frenck, L.; Sethi, G. K.; Maslyn, J. A.; Balsara, N. P. Factors That Control the Formation of Dendrites and Other Morphologies on Lithium Metal Anodes. *Front. Energy Res.* **2019**, *7*, 115. https://doi.org/10.3389/fenrg.2019.00115.

(44) Barai, P.; Higa, K.; Srinivasan, V. Impact of Electrolyte Transference Number on Lithium Dendrite Growth Process. *ECS Meet. Abstr.* **2017**, *MA2017-02*. https://doi.org/10.1149/MA2017-02/1/66.

(45) Jana, A.; Woo, S. I.; Vikrant, K. S. N.; García, R. E. Electrochemomechanics of Lithium Dendrite Growth. *Energy Environ. Sci.* **2019**, *12* (12), 3595–3607. https://doi.org/10.1039/C9EE01864F.

(46) Chen, K.-H.; Wood, K. N.; Kazyak, E.; LePage, W. S.; Davis, A. L.; Sanchez, A. J.; Dasgupta, N. P. Dead Lithium: Mass Transport Effects on Voltage, Capacity, and Failure of Lithium Metal Anodes. *J. Mater. Chem. A* **2017**, *5* (23), 11671–11681. https://doi.org/10.1039/C7TA00371D.

(47) Wood, K. N.; Kazyak, E.; Chadwick, A. F.; Chen, K.-H.; Zhang, J.-G.; Thornton, K.; Dasgupta, N. P. Dendrites and Pits: Untangling the Complex Behavior of Lithium Metal Anodes through Operando Video Microscopy. *ACS Cent. Sci.* **2016**, *2* (11), 790–801. https://doi.org/10.1021/acscentsci.6b00260.

(48) Swamy, T.; Park, R.; Sheldon, B. W.; Rettenwander, D.; Porz, L.; Berendts, S.; Uecker, R.; Carter, W. C.; Chiang, Y.-M. Lithium Metal Penetration Induced by Electrodeposition through Solid Electrolytes: Example in Single-Crystal $Li_6La_3ZrTaO_{12}$ Garnet. *J. Electrochem. Soc.* **2018**, *165* (16), A3648–A3655. https://doi.org/10.1149/2.1391814jes.

(49) Sharon, D.; Bennington, P.; Patel, S. N.; Nealey, P. F. Stabilizing Dendritic Electrodeposition by Limiting Spatial Dimensions in Nanostructured Electrolytes. *ACS*

Energy Lett. **2020**, *5* (9), 2889–2896. https://doi.org/10.1021/acsenergylett.0c01543.

(50) Li, S.; Fang, S.; Dou, H.; Zhang, X. RbF as a Dendrite-Inhibiting Additive in Lithium Metal Batteries. *ACS Appl. Mater. Interfaces* **2019**, *11* (23), 20804–20811. https://doi.org/10.1021/acsami.9b03940.

(51) Mehdi, B. L.; Qian, J.; Nasybulin, E.; Park, C.; Welch, D. A.; Faller, R.; Mehta, H.; Henderson, W. A.; Xu, W.; Wang, C. M.; Evans, J. E.; Liu, J.; Zhang, J.-G.; Mueller, K. T.; Browning, N. D. Observation and Quantification of Nanoscale Processes in Lithium Batteries by Operando Electrochemical (S)TEM. *Nano Lett.* **2015**, *15* (3), 2168–2173. https://doi.org/10.1021/acs.nanolett.5b00175.

(52) Mehdi, B. L.; Stevens, A.; Qian, J.; Park, C.; Xu, W.; Henderson, W. A.; Zhang, J.-G.; Mueller, K. T.; Browning, N. D. The Impact of Li Grain Size on Coulombic Efficiency in Li Batteries. *Sci. Rep.* **2016**, *6* (1), 34267. https://doi.org/10.1038/srep34267.

(53) Matsen, M. W.; Bates, F. S. Unifying Weak- and Strong-Segregation Block Copolymer Theories. *Macromolecules* **1996**, *29* (4), 1091–1098. https://doi.org/10.1021/ma951138i.

(54) Pandolfi, R. J.; Allan, D. B.; Arenholz, E.; Barroso-Luque, L.; Campbell, S. I.; Caswell, T. A.; Blair, A.; De Carlo, F.; Fackler, S.; Fournier, A. P.; Freychet, G.; Fukuto, M.; Gürsoy, D.; Jiang, Z.; Krishnan, H.; Kumar, D.; Kline, R. J.; Li, R.; Liman, C.; Marchesini, S.; Mehta, A.; N'Diaye, A. T.; Parkinson, D. Y.; Parks, H.; Pellouchoud, L. A.; Perciano, T.; Ren, F.; Sahoo, S.; Strzalka, J.; Sunday, D.; Tassone, C. J.; Ushizima, D.; Venkatakrishnan, S.; Yager, K. G.; Zwart, P.; Sethian, J. A.; Hexemer, A. Xi-Cam: A Versatile Interface for Data Visualization and Analysis. *J. Synchrotron Radiat.* **2018**, *25* (4), 1261–1270. https://doi.org/10.1107/S1600577518005787.

FOR TABLE OF CONTENTS ONLY